Supporting Online Material for

Lysosomal Pathology and Osteopetrosis upon Loss of H^+-Driven Lysosomal Cl^- Accumulation

Stefanie Weinert, Sabrina Jabs, Chayarop Supanchart, Michaela Schweizer, Niclas Gimber, Martin Richter, Jörg Rademann, Tobias Stauber, Uwe Kornak, Thomas J. Jentsch*

*To whom correspondence should be addressed. E-mail: jentsch@fmp-berlin.de

Published 29 April 2010 on *Science* Express
DOI: 10.1126/science.1188072

This PDF file includes:

Materials and Methods

Mice

The generation of *Clcn7*$^{-/-}$ mice has been described previously (*1*). Grey-lethal (*Ostm1*$^{-/-}$) mice (*2*) were obtained from the Jackson laboratories. For the generation of *Clcn7*$^{unc/unc}$ mice 8 kb of mouse genomic sequence extending from exon 6 to 16 of *Clcn7* were amplified from R1 ES cells and cloned into pKO Scrambler plasmid 901 (Lexicon Genetics Incorporated) containing a dtA cassette (diphtheria toxin A cassette). A neomycin (neo) resistance cassette flanked by FRT sites was introduced between exon 7 and 8 to select for recombination in embryonic stem (ES) cells. Exon 9 was modified by inserting the uncoupling E245A mutation and removing a *Bam*HI restriction site through a silent mutation. The targeting construct was completely sequenced on ABI 3730 DNA analyzer (Applied Biosystems). Targeted R1 ES cells were screened by Southern Blot analysis using *Bam*HI and an external 1.0-kb probe. Correctly targeted ES cells were injected into C57Bl/6 blastocysts. Chimeric animals were crossed with FLPe-recombinase-expressing 'deleter' mice (*3*) and resulting heterozygous animals (*Clcn7*$^{+/unc}$) were inbred to yield *Clcn7*$^{unc/unc}$. Exon 9 of the genomic *Clcn7*$^{unc/unc}$ gene was amplified with intronic primers and sequenced. Experiments were performed with mice in a mixed C57Bl/6-129/Svj genetic background, always using littermates as controls.

Antibodies

Primary antibodies were: rabbit / guinea pig anti-ClC-7 (*1*), rabbit / guinea pig anti-Ostm1 (*4*), rabbit anti-ClC-5 (PEP5A) (*5*), rabbit anti-ClC-3 (ab#1036) (*6*), mouse anti-villin (Acris), rabbit anti-ClC-6 (*7*), rat anti-Lamp-1 (clone 1D4B; BD Pharmingen), mouse anti-GFAP (Roche), rabbit anti-β-actin (Sigma-Aldrich), mouse anti-VAMP2 (Synaptic Systems) and mouse anti-FITC (clone FL-D6; Sigma-Aldrich). Secondary antibodies were coupled to Alexa Fluor 488, 546, 633 (Invitrogen) or HRP (Jackson ImmunoResearch). GSA-biotin (*Griffonia simplicifolia* agglutinin, Vector Laboratories) was detected using Streptavidin-FITC (Sigma-Aldrich).

Membrane preparation and immunoblot

Tissues were homogenized in PBS with protease inhibitors (Complete® protease inhibitor cocktail, Roche) and cleared by centrifugation at 1,000 x g for 10 min. Membranes were pelleted at 270,000 x g for 30 min and subsequently resuspended in PBS supplemented with protease inhibitors and 2% (w/v) SDS. Equal amounts of protein were separated by SDS–PAGE and blotted onto nitrocellulose.

Histology and electron microscopy

Deeply anesthetized mice were perfused with 4% (w/v) PFA in PBS and isolated tissues postfixed overnight at 4°C. Tibiae were dec alcified for 4 days in 10% (w/v) EDTA in PBS and again postfixed. 8-µm paraffin sections of the brain were used for Nissl and periodic acid Schiff (PAS) staining and 8-µm cryosections for immunohistochemistry and lysosomal acid phosphatase assay. Lysosomal acid phosphatase activity in situ was determined using β-glycerophosphate as a substrate. Cryosections were incubated for 2 h at 37°C in 0.3% (w/v) sodium- β-glycerophosphate with 0.125% (w/v) lead nitrate in 50 mM acetate buffer pH 5.0. After washing, sections were stained with 0.1% (w/v) ammonium sulfide for 1 min. No staining was observed when substrate was omitted. For immunohistochemistry, sections were postfixed with 4% (w/v) PFA, permeabilized using 0.2% (v/v) Triton X-

100 in PBS and blocked with 3% (w/v) BSA in PBS. Antibody incubation was in blocking buffer. For ClC-7, an antigen retrieval step (10 min in sodium citrate buffer, pH 6.0, at 95 ℃) was included after fixation. For immunocytochemistry, fibroblasts were seeded onto glass coverslips, fixed for 12 min with 4% (w/v) PFA, permeabilized with 0.1% (w/v) saponin and blocked with 3% (w/v) BSA in PBS. Antigen retrieval on fibroblasts was not necessary. Confocal images were acquired with an LSM 510 (Zeiss).

For electron microscopy, mice were perfused with 4% (w/v) PFA and 1% (v/v) glutaraldehyde in 0.1 M phosphate buffer (pH 7.4). Brains were cut in 150-µm sagittal sections with a vibratome. The eyes were opened at the crystalline lens and the vitreous humor removed. Tibiae were decalcified with 10% (w/v) EDTA in PBS for 3 to 4 days. Thin slices were prepared and postfixed in 1% (v/v) OsO_4, dehydrated and embedded in epon. Semi-thin sections (0.5 µm) were labeled with methylene blue. Ultrathin sections (60 nm) were stained with uranyl acetate and lead citrate and examined with a Zeiss EM 902.

For non-decalcified sections, tibiae were fixed in 4% (w/v) PFA for 24 h at 4℃. After washing in PBS specimen were dehydrated in ethanol, followed by incubation in 50% ethanol in acetone for 12 h. After further washing in ethanol and xylene, bones were embedded in methylmethacrylate (Merck). 4-µm sections were prepared using a Leica RM2255 microtome. After incubating sections in 2-methoxyethyl acetate (Merck) and rehydration, sections were at first stained according to the von Kossa protocol, followed by Goldner trichrome staining.

Micro-CT and Radiographs

For micro-CT (Computed Tomography) and contact radiography a Viva CT40 scanner (Scanco Medical) and an Mx20 (Faxitron) were used, respectively.

Cell culture

Mouse adult fibroblasts from *Clcn7*$^{unc/unc}$, *Clcn7*$^{+/unc}$, *Clcn7*$^{-/-}$ and WT mice were prepared by dissociation of tail biopsies with collagenase/dispase and cultured in DMEM containing 10% (v/v) fetal calf serum. Each cell line was generated from a different animal.

Osteoclast differentiation and resorption assays

Osteoclast progenitor cells were isolated from spleen and incubated for 15 h in OC-medium (alphaMEM (Lonza), 10% (v/v) FCS (Gibco), 2 mM Ultraglutamine (Lonza), 1% (w/v) penicillin/streptomycin (Gibco)). For resorption assays $8x10^5/cm^2$ non-adherent cells were seeded onto dentine slices that had been seeded with $10^4/cm^2$ primary calvarial osteoblasts the day before and grown for two days in co-culture medium (OC-medium containing 10^{-8} M vitamin D (Sigma-Aldrich), 10^{-8} M dexamethasone (Sigma-Aldrich) and 10 ng/ml M-CSF (R&D)). At days 2, 5 and 8 the medium was replaced by co-culture medium containing 20 ng/ml sRANKL (Peprotech). Dentine slices were cleaned by 1% (w/v) SDS and then stained with WGA lectin/Texas Red (Vector) in 1% (w/v) BSA/1x PBS for confocal microscopy of pit depth, followed by Indian ink staining to quantify pit numbers. For differentiation assays, $8x10^5/cm^2$ non-adherent cells were seeded on glass coverslips and cultured with OC-medium supplemented with 15 ng/ml M-CSF for two days and with 15 ng/ml M-CSF and 50 ng/ml sRANKL for six days with medium change after three days. Cells were fixed with 4% (w/v) PFA and subjected to tartrate-resistant acid phosphatase (TRAP) staining, followed by phalloidin/Alexa Fluor 488 (Invitrogen) and

DAPI (Invitrogen) staining. TRAP-positive cells with actin rings and more than two nuclei were counted as osteoclasts.

Determination of lysosomal pH

Lysosomal pH was measured by ratiometric fluorescence imaging of the pH sensor Oregon-Green 488 (Invitrogen). The fluorophore coupled to 10-kDa dextran (Invitrogen) was specifically targeted to lysosomes using a standard pulse-chase protocol. In detail, primary cultures of fibroblasts from *Clcn7*$^{unc/unc}$, *Clcn7*$^{+/unc}$, *Clcn7*$^{-/-}$ and WT mice were plated onto glass coverslips and loaded overnight with 0.3 mg/ml pH dye in growth medium. Cells were washed and Oregon Green-dextran chased into lysosomes for 2 h at 37°C in serum-supplemented growth medium. Control experiments indicated that the dye was localized to Lamp1-positive vesicles. Ratiometric fluorescence images were acquired using an inverted microscope (Zeiss Axiovert 200 equipped with a 100x 1.30 NA oil immersion lens) connected to a Polychrom II monochromator (TILL photonics) at excitation wavelengths of 440 and 488 nm, respectively. The emitted light was filtered with a 535 ± 20-nm filter and captured with a Sensicam CCD camera (PCO). For each genotype, at least 3 different cells from 3 independent cell lines with at least 10 single lysosomes each were measured in Ringer solution (in mM: 140 NaCl, 3 KCl, 2 K_2HPO_4, 1 $CaCl_2$, 1 $MgSO_4$, 5 HEPES, 10 glucose, pH 7.4). Image analysis was performed with the Vision software package (TILL photonics). Regions of interest (ROI) were defined as areas above a defined fluorescence threshold in the acquired images at 488-nm excitation. The mean intensity ratio between 488- and 440-nm excitation was calculated for each ROI.

At the end of each experiment, in situ pH calibration curves were obtained after treatment in isotonic K^+-based solutions (in mM: 5 NaCl, 115 KCl, 1.2 $MgSO_4$, 10 glucose, 25 of either HEPES or MES) ranging in pH from 3.9 through 6.45 supplemented with 1 mM of both nigericin and monensin (both Sigma-Aldrich). Cells were equilibrated for at least 2 min for each pH value. The resulting fluorescence intensity ratio (488/440) as a function of pH was fit to a sigmoid and used to interpolate pH values from the experimental ratio data.

In vitro measurement of ATP-dependent acidification

Fibroblasts were seeded on 3.5-cm cell culture dishes and loaded overnight with 0.5 mg/ml fluorescein-dextran, followed by a chase of 2-4 h in serum-supplemented growth medium. The cells were washed with homogenization buffer (in mM: 90 K-gluconate, 50 KCl, 1 EGTA, 5 HEPES pH 7.2, 50 sucrose, Complete® protease inhibitor cocktail) prior to treatment with 1 µM FCCP (Sigma-Aldrich) for 15 min in order to dissipate the lysosomal pH gradient. The FCCP-treated cells were homogenized with a Dounce homogenizer (tight pestle), unbroken cells and nuclei were removed by spinning at 1,000 x g for 5 min and endomembranes were pelleted from the supernatant by centrifugation at 18,000 x g at 4°C for 20 min. The endomembrane pellet was washed once with homogenization buffer and resuspended in 600 µl of homogenization buffer additionally containing 2 µl of anti-FITC antibody to quench extravesicular fluorescence (*8*).

Fluorescence was monitored with a Xenius spectrofluorometer (Safas) sequentially at two excitation wavelengths (490 nm and 440 nm, emission 530 nm). Following a baseline measurement, 2 mM Mg-ATP was added while continuously monitoring the fluorescence. Lysosomes were re-alkalinized with 10 µM nigericin. For Cl^--free conditions, KCl was replaced by K-gluconate. As control, ATP-dependent acidification was inhibited by 500 nM concanamycin A (Sigma-Aldrich).

In vitro measurement of Cl^--driven H^+-transport

Fluorescein-dextran-labeled endomembranes were prepared as described above. The endomembrane pellet was resuspended in 150 µl of a low-chloride buffer (in mM: 10 KCl, 20 K-gluconate,110 NMDG-gluconate, 50 sucrose, 1 EGTA, Complete® protease inhibitor cocktail) containing 1% (w/v) BSA, 10 HEPES pH 7.2 and added to 450 µl of either the low-chloride buffer additionally containing 10 µM valinomycin (Sigma-Aldrich) or 450 µl of high-chloride buffer (as above except with all the gluconate replaced with chloride), also containing 10 µM valinomycin. Solutions additionally contained 3 mM Mg-ATP because it is not known whether ClC-7 requires nucleotide-binding for regulatory or structural reasons, analogous to ClC-5 (*9*). It also contained 500 nM concanamycin A to inhibit the vacuolar H^+-ATPase. Final Cl^- concentrations are 10 mM and 107 mM, respectively. Ratiometric pH measurements were carried out as described above.

In vivo measurement of CCCP-mediated alkalinization

Lysosomes of fibroblasts were loaded with Oregon-Green-dextran using the pulse-chase protocol as above. Cells were equilibrated with Ringer solution for 10 min. Alkalinization was initiated after 5 s by applying Ringer solution containing 200 µM CCCP (Sigma-Aldrich). Images were acquired for 55 s and analyzed as above. Experimenters were blinded to the genotype.

Synthesis of MEQ-TMR-dextran as a ratioable Cl^- indicator

Synthesis of N-(7-carboxyhexyl)-6-methoxy-quinolinium bromide: 6-Methoxyquinoline (0.993 ml, 7.2 mM) and 8-bromooctanoic acid (1.606 g, 7.2 mM) were heated under reflux at 110 °C for 14 h. After cooling to room temperature (RT) acetone (50 ml) was added, the mixture was agitated in an ultrasound bath for 1 h and then stirred for another 16 h. The precipitated solid was centrifuged and washed several times with diethyl ether and dried in vacuo yielding 2.1 g (76 %) of a white solid.

Synthesis of N-(7-(N-succinimidyl)-oxycarbonyl-heptyl)-6-methoxy-quinolinium bromide (MEQ-OSu): N-(7-carboxyhexyl)-6-methoxy-quinolinium bromide (1 g, 2.616 mM), N-hydroxysuccinimide (0.903 g, 7.848 mM) and N,N-dicyclohexylcarbodiimide (1.349 g, 6.54 mM) were dissolved in DMF (45 ml) and stirred for 24 h at RT. The solvent was evaporated in vacuo, acetonitrile (10 ml) was added, and the mixture was stirred for 1 h. The precipitate was then removed by filtration, the filtrate was concentrated in vacuo and added dropwise to a strongly stirred solution of ethyl acetate/ hexane (500 ml, 3:1 v/v). The precipitated product was redissolved in DMF and precipitated in ethyl acetate/ hexane (500 ml, 3:1 v/v) again. After drying a yellowish solid (1.254 g, 99 %) was obtained.

Synthesis of carboxyethyl dextran (CED): Dextran (5 g, 0.5 mM, MW 10 kDa, Sigma-Aldrich) was dissolved in of 1 N NaOH solution (50 ml). Acryl amide (0.9 g, 12.5 mM) was added and stirred at 30 °C. After 24 h the reaction temperature was increased to 50 °C and stirred for 24 h. The solution was neutralized, dialyzed against 0.1 N HCl and water. After lyophilization a white powder was obtained (4 g, 72 %, 13 carboxyethyl groups per dextran unit).

Synthesis of N-(2-Aminoethyl)-aminocarbonyl-ethyl dextran (AAE-dextran): CED (1 g, 0.1 mM, loaded with 13 CE groups) and ethylenediamine (0.792 ml, 11.827 mM) were dissolved in water (5 ml). The pH was adjusted to 6. N-(3-dimethylaminopropyl)-N-ethyl carbodiimide (1.134 g, 5.914 mM) was added and the solution was stirred for 4 h. Solvents were evaporated and the residue was washed with methanol and DMF several times. The white precipitate was dissolved in water and purified over a

Sephadex G15 column. After lyophilization 0.8 g (76 %, ~13 amino groups per dextran unit) of pure white product were obtained.
Synthesis of ratioable MEQ-TMR-dextran: AAE-dextran (36 mg, 0.003 mM, ca. 0.039 mM amino groups) and 5,6-(N-succinimidyl-oxycarbonyl)-N,N,N´,N´-tetramethyl-rhodamine (TMR-OSu) (3 mg, 0.007 mM, Invitrogen) were dissolved in water (2 ml) and were stirred at pH 8.5. After 2 h MEQ-OSu (22 mg, 0.046 mM) was added and the mixture was stirred for 16 h. After concentrating the solution in vacuo the product was precipitated with methanol. Washing several times with DMF and methanol yielded a red solid which was dissolved in water and purified over Sephadex G15. (40 mg, 77.5 %, 2 TMR and 11 MEQ groups per dextran unit). All products were verified by NMR. Relevant NMR data can be obtained from the authors upon request.

Characterization of the Cl^--sensitive dye
Detailed chloride quenching characteristics for uncoupled MEQ have been published before (*10*). Fluorescence spectra of MEQ/TMR-dextran were measured using a Xenius spectrofluorimeter (Safas). Fluorescence quenching experiments were carried out at 360 nm excitation and 440 nm emission wavelength for the MEQ moiety and 524 nm and 580 nm for TMR. Aliquots of either NaCl or Na-gluconate stock solutions were added to a 20 µg/ ml solution of MEQ/TMR-dextran in 10 mM HEPES pH 7.4 and fluorescence spectra measured. The fluorescence ratio was calculated from fluorescence intensity at emission peaks. For pH-dependency experiments, the same amount of MEQ/TMR-dextran was added to 10 mM MES or HEPES buffered solutions ranging from pH 4 to 7.4, additionally containing 5 mM NaCl.

Determination of lysosomal chloride concentration
Lysosomal chloride was measured by ratiometric fluorescence life cell imaging of MEQ/ TMR-dextran, which was targeted to lysosomes using a standard pulse-chase protocol. Primary cultures of fibroblasts from $Clcn7^{unc/unc}$, $Clcn7^{-/-}$ and WT mice were plated onto glass-bottom culture dishes (MatTek) and loaded for 1h with 20 mg/ml dye in growth medium. Cells were washed and MEQ/TMR-dextran chased into lysosomes for 2 h at 37℃ in NaCl-free IMDM (Iscove's Modified Dulbecco's Medium; PAN-Biotech) with remaining [Cl^-] of 7 mM. Ratiometric fluorescence images at excitation wavelengths of 360 and 524 nm, respectively, were acquired using an inverted microscope (Zeiss Axiovert 200 equipped with a 100x 1.30 NA oil immersion lens) connected to a Polychrom II monochromator (TILL photonics) and a Lambda 10-2 emission filter wheel (Sutter Instruments). The emitted light was filtered with a 440 ± 20 nm or 580 ± 20 nm filter and captured with a Sensicam CCD camera (PCO). For each genotype, 10 dishes with 10 different cells from at least 3 independent primary cell lines were measured in imaging buffer (in mM: Na-gluconate 135 mM Na-gluconate 5 KCl, 1 $CaCl_2$, 1 $MgCl_2$, 10 HEPES, 10 glucose, pH 7.4). Image analysis was performed with the Vision software package (TILL photonics). For each cell, 10 lysosomes were chosen as regions of interest (ROI). The mean intensity ratio between 360- and 524-nm excitation was calculated for each ROI after background subtraction.

Mathematical modeling of vesicular ion transport
In order to roughly estimate changes in lysosomal ion concentrations and membrane potential, a set of ordinary differential equations describing changes in these parameters were solved by numerical integration. Since only some parameters have been determined here or have been described in the literature, others had to be estimated and adapted to obtain reasonable results. Our model contains several

simplifications compared to published, more sophisticated models (*11, 12*) (which have not considered Cl^-/H^+-exchange though) and serves merely as a valuable plausibility check for the interpretation of our experimental data.

Vesicles (lysosomes) were modeled with a volume $V_{ves}= 0.52*10^{-15}$ l and a surface area $A_{ves}= 3.14\ \mu m^2$ (corresponding to a sphere with a diameter of 1 µm). Assuming that the typical specific capacitance of biological membranes of 1 $\mu F/cm^2$ also holds for lysosomes, the electrical capacitance of the vesicle was set to $C_{ves}=$ 0.0314 pF. In addition to fix negative charges A^- within lysosomes (representing e.g. proteins), our simplified model considers three ionic species, i.e. Cl^-, H^+, and unspecific monovalent cations (cat). The extravesicular concentrations of these ions (indicated by subscript o, e.g. $[Cl^-]_o$) were set as constant during virtual experiments. Because protons are largely sequestered by buffering, we define a free proton concentration $[H^+_{free}]$ and a total proton concentration $[H^+_{tot}]$. These are related to each other by the buffer capacity β

(1) $\Delta pH = \Delta[H^+_{tot}]/\beta$

and

(2) $[H^+_{free}] = 10^{-pH}$.

The buffer capacity was set to β = 30 mM/pH unit according to published values (*8*). For simplicity, in our model both β and $[A^-]$ were set as constant, although they will depend on pH in real life. Changes in osmolarity were ignored.

The vesicular membrane potential (with outside being 0 by definition) is calculated to

(3) $U = ([cat^+]_i + [H^+_{tot}]_i - [Cl^-]_i - [A^-]_i)* V_{ves} *F/C_{ves}$,

with F being Faraday's constant and subscript i denotes the luminal compartment.

The following transport processes were included, in various combinations, in our model calculations:

H^+-flux by V-type H^+-ATPase:

(4) $J_{H,\ ATPase} = - (U - (RT/F)*(\ln([H^+_{free}]_o/[H^+_{free}]_i) - U_{ATP}) * g_{ATPase}$

with R being the gas constant, T the absolute temperature (300 K), U_{ATP} the electrochemical potential provided by ATP hydrolysis (U_{ATP} = 270 mV) (*11*), and g_{ATPase} is a scaling factor reflecting the number of active pumps in the membrane.

H^+- and Cl^--flux, respectively, by CLC $2Cl^-/H^+$-exchangers:

(5) $J_{H,\ CLC(WT)} = -(U - (RT/3F)*\ln(([H^+_{free}]_o/[H^+_{free}]_i)([Cl^-]_i^2/[Cl^-]_o^2))) * g_{CLC}$

(6) $J_{Cl,\ CLC(WT)} = 2*(U - (RT/3F)*\ln(([H^+_{free}]_o/[H^+_{free}]_i)([Cl^-]_i^2/[Cl^-]_o^2))) * g_{CLC}$

with g_{CLC} being a scaling factor reflecting the number of active CLC transporters in the membrane.

Cl^--flux through $ClC\text{-}7^{unc}$ or any other type of ohmic Cl^--conductance:

(7) $J_{Cl,\ cond} = (U + (RT/F)\ln([Cl^-]_o/[Cl^-]_i)) * g_{Cl,\ cond}$

H^+-flux through an 'H^+-leak':

(8) $J_{H,\ cond} = (-U + (RT/F)\ln([H^+_{free}]_o/[H^+_{free}]_i)) * g_{H,\ cond}$

Cation-flux through unspecied cation-conductances, respectively:

(9) $J_{cat,\ cond} = (-U + (RT/F)\ln([cat^+]_o/[cat^+]_i)) * g_{cat,\ cond}$

Changes in ion concentrations are then described by:

(10) $d[H^+_{tot}]_i/dt = J_{H,\ ATPase} + J_{H,\ CLC(WT)} + J_{H,\ cond}$

(11) $d[Cl^-]_i/dt = J_{Cl,\ CLC(WT)} + J_{Cl,\ cond}$

(12) $d[cat^+]_i/dt = J_{cat,\ cond}$

This set of differential equations was solved by numerical integration using the VCell program suite (Version 4.7 beta; Virtual Cell Resource, National Resource for Cell Analysis and Modeling, University of Connecticut Health Center) using the combined stiff solver (IDA/CVODE) as numerical integrator. When certain transport processes were not considered, the respective scaling factor g was set to zero. Results were exported to Excel for further analysis and display.

Supporting Figures

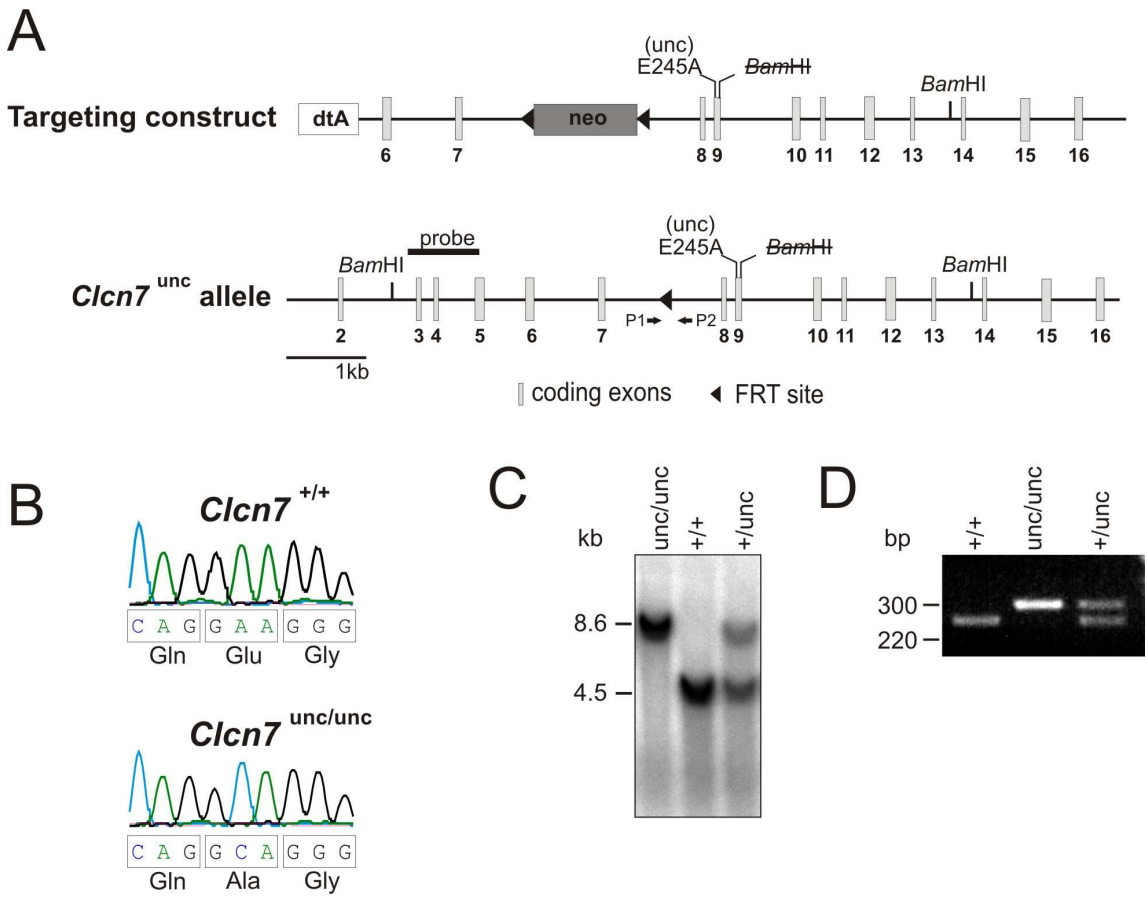

Fig. S1. Generation of *Clcn7*$^{unc/unc}$ mice. (**A**) Gene targeting strategy. Top diagram, targeting construct that contains 8 kb of mouse genomic sequence starting from exon 6 through 16 and a dtA (diphtheria toxin A) cassette. Exon 9 was modified by inserting the uncoupling E245A mutation and additionally a silent mutation to remove a *Bam*HI restriction site which was subsequently used for Southern blot analysis. A neomycin (neo) resistance cassette flanked by FRT sites was introduced between exons 7 and 8 to select for recombination in embryonic stem (ES) cells. Correctly targeted ES cells were injected into blastocysts. Chimeric animals were crossed with FLPe-recombinase-expressing 'deleter' mice (*3*) resulting in the **unc**oupled *Clcn7*^{unc} allele (bottom). (**B**) DNA sequence obtained from homozygous *Clcn7*^{unc} mice confirms the presence of the E245A mutation. (**C, D**) Southern blot analysis (C) and PCR (D) on mouse genomic DNA used for genotyping with the hybridization probe and PCR primers, respectively, indicated in (A). For Southern blot analysis, genomic DNA was digested with *Bam*HI. The sequences of PCR primers were for P1: 5' TATCTCAGAAGGCAGGTAGG 3' and for P2: 5' AGTCTGTTAGCCAGAGGTAG 3'.

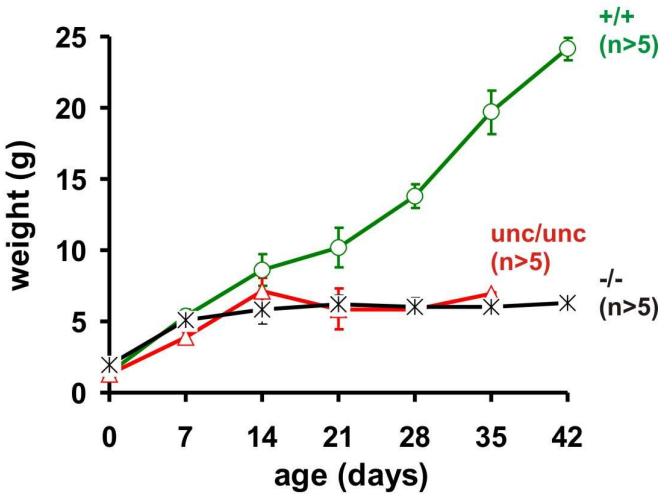

Fig. S2. Similar growth retardation in *Clcn7*$^{unc/unc}$ and *Clcn7*$^{-/-}$ mice compared to *Clcn7*$^{+/+}$ mice. *Clcn7*$^{unc/unc}$ mice died within ~5 weeks after birth, whereas *Clcn7*$^{-/-}$ mice survived until 6-7 weeks after birth.

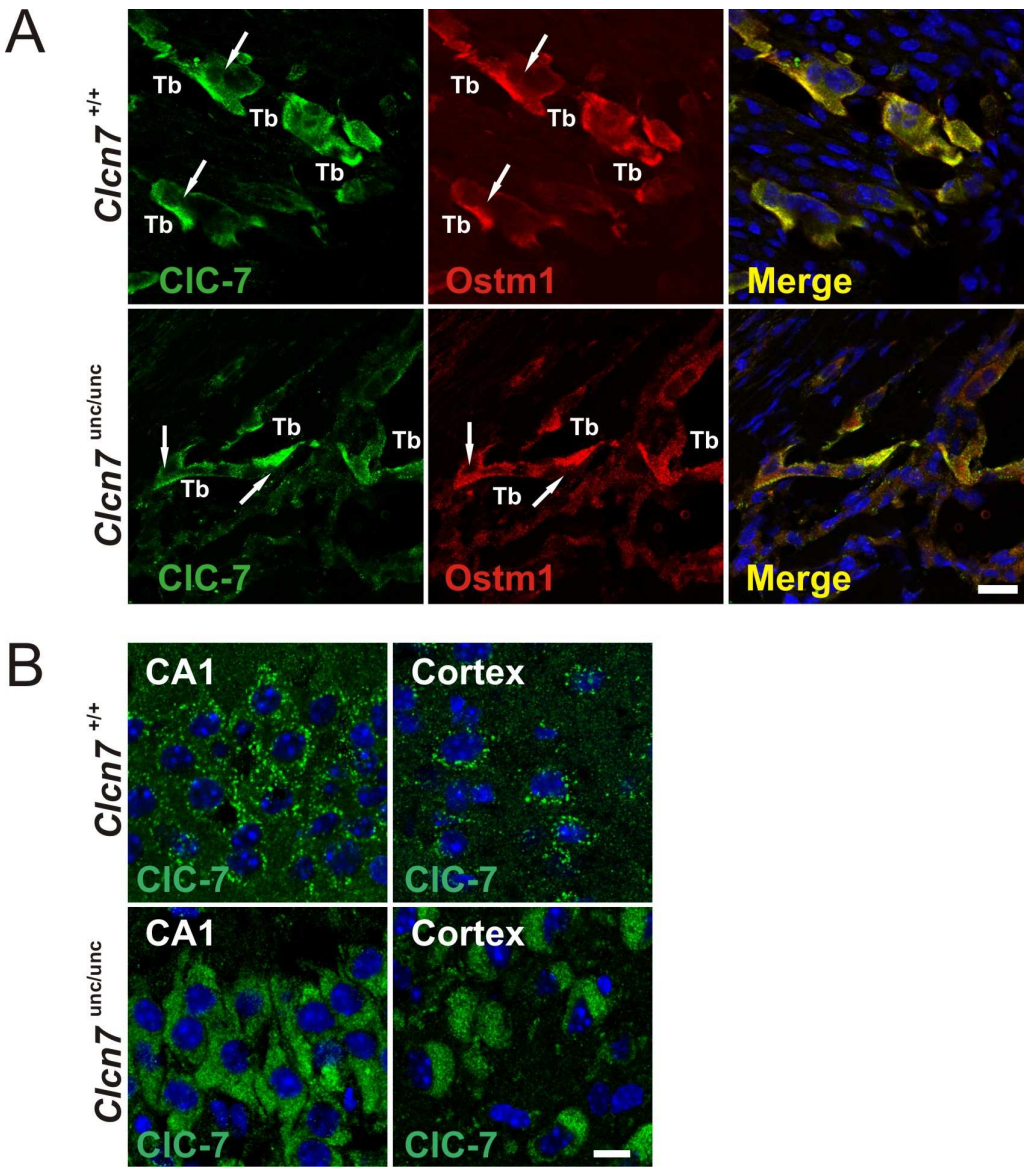

Fig. S3. Localization of ClC-7^{unc} and Ostm1 in *Clcn7*$^{unc/unc}$ mice. (**A**) Immunostaining for ClC-7 and Ostm1 in bone. Both proteins show a dense overlapping staining in osteoclasts which is apposed to trabecles (arrows) and reflects ruffled borders. Note that osteoclasts are thinner in *Clcn7*$^{unc/unc}$ than in WT mice (Tb= trabecle). (**B**) Immunohistochemistry shows vesicular localization of ClC-7 in the hippocampal CA1 region and cortex of the WT brain but a more diffuse staining of ClC-7^{unc} in the hippocampus and cortex of *Clcn7*$^{unc/unc}$ brain. Scale bars: 20 µm (A) and 10 µm (B).

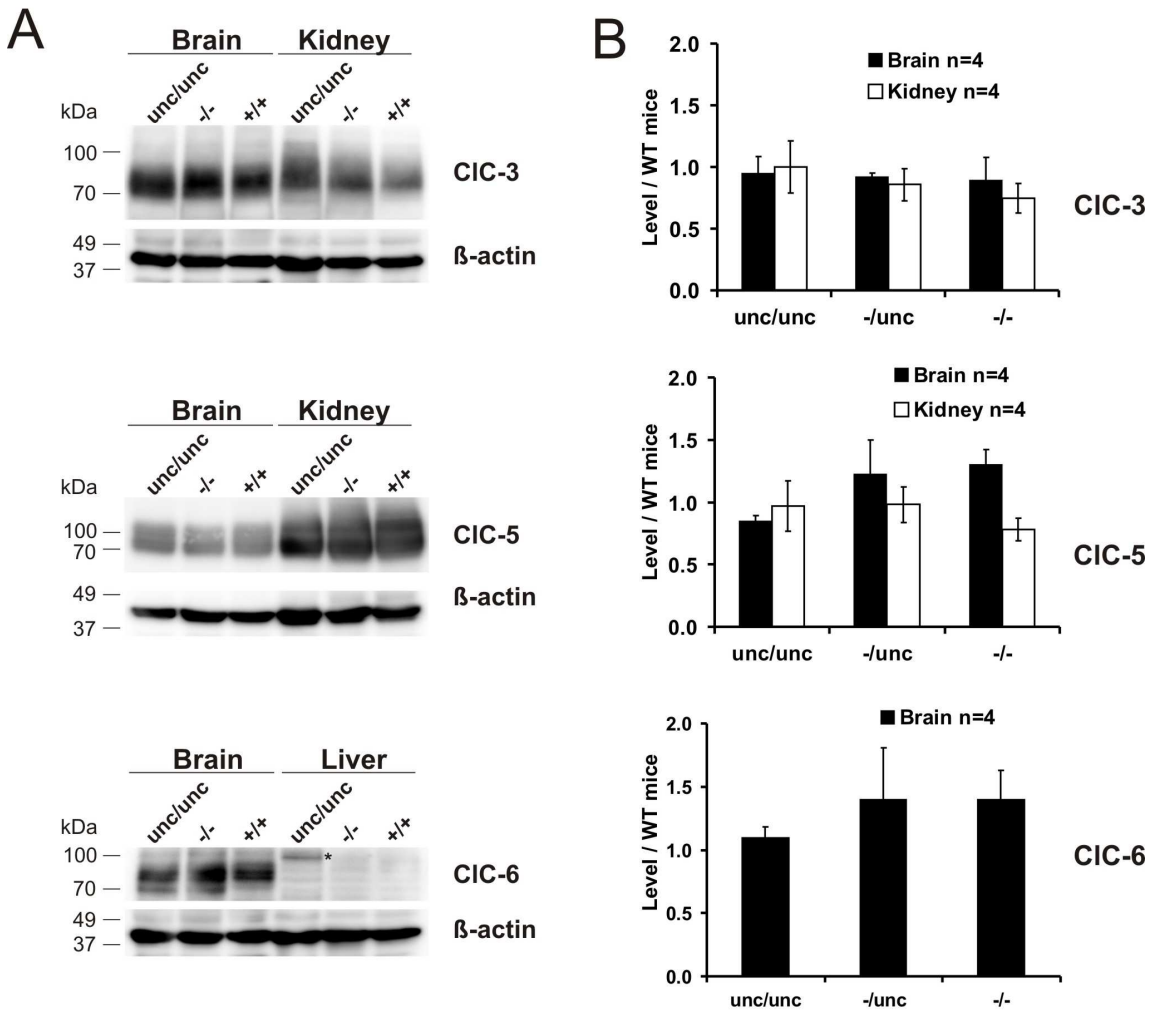

Fig. S4. Unchanged abundance of other vesicular CLC proteins in *Clcn7*$^{unc/unc}$ mice. (**A, B**) Immunoblots (A) and subsequent quantifications (B) reveal unchanged levels of ClC-3 and ClC-5 in brain and kidney of *Clcn7*$^{unc/unc}$, *Clcn7*$^{-/unc}$ and *Clcn7*$^{-/-}$ mice. ClC-6 is not expressed in liver but also shows a similar expression in brain of *Clcn7*$^{unc/unc}$, *Clcn7*$^{-/unc}$ and *Clcn7*$^{-/-}$ mice when compared to WT. Note that ClC-6 gives a band at ~ 80 kDa. Asterisk indicates a non-specific band. Signals were normalized to β-actin that was used as loading control.

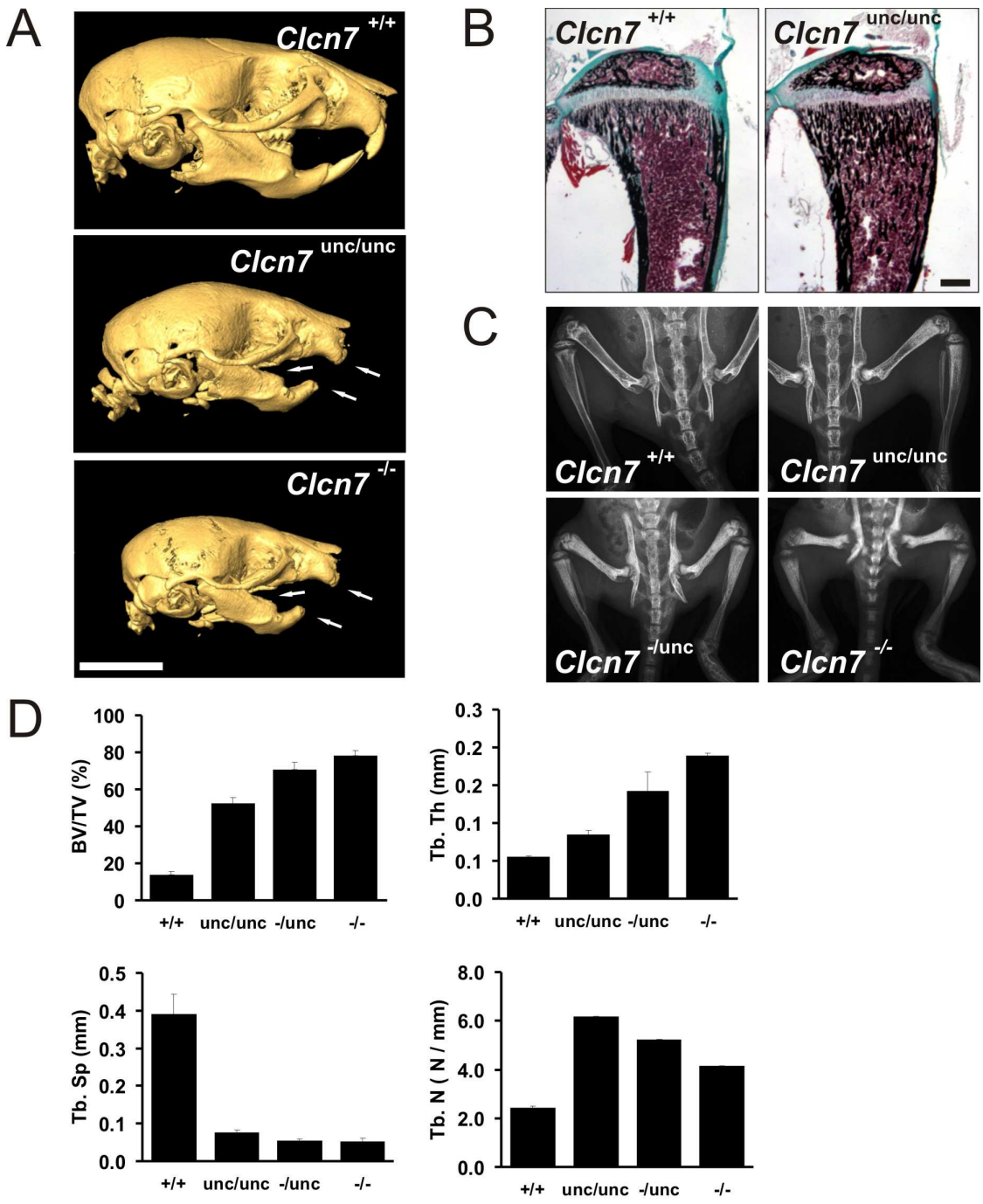

Fig. S5. Bone phenotype of *Clcn7*$^{unc/unc}$ mice. (**A**) 3D micro-CT images of skulls from P21 animals. Skulls of *Clcn7*$^{unc/unc}$ and *Clcn7*$^{-/-}$ mice are smaller and show impaired tooth eruption (arrows). (**B**) Goldner trichrome/von Kossa staining of non-decalcified tibiae shows normal morphology and growth plate thickness but elevated trabecular bone density in primary and secondary spongiosa of *Clcn7*$^{unc/unc}$ sections. (**C**) X-ray of P22 mouse skeletons reveals increasing bone density from WT to *Clcn7*$^{unc/unc}$, *Clcn7*$^{-/unc}$ and *Clcn7*$^{-/-}$ mice. (**D**) Quantification of tibial trabecular bone by micro-CT. Bone volume fraction (BV/TV), trabecular thickness (Tb.Th) and trabecular number (Tb.N) increase while trabecular separation (Tb.Sp) decreases from WT over *Clcn7*$^{unc/unc}$ to *Clcn7*$^{-/unc}$ and is minimal for *Clcn7*$^{-/-}$. Scale bars: 10 mm (A) and 0.5 mm (B).

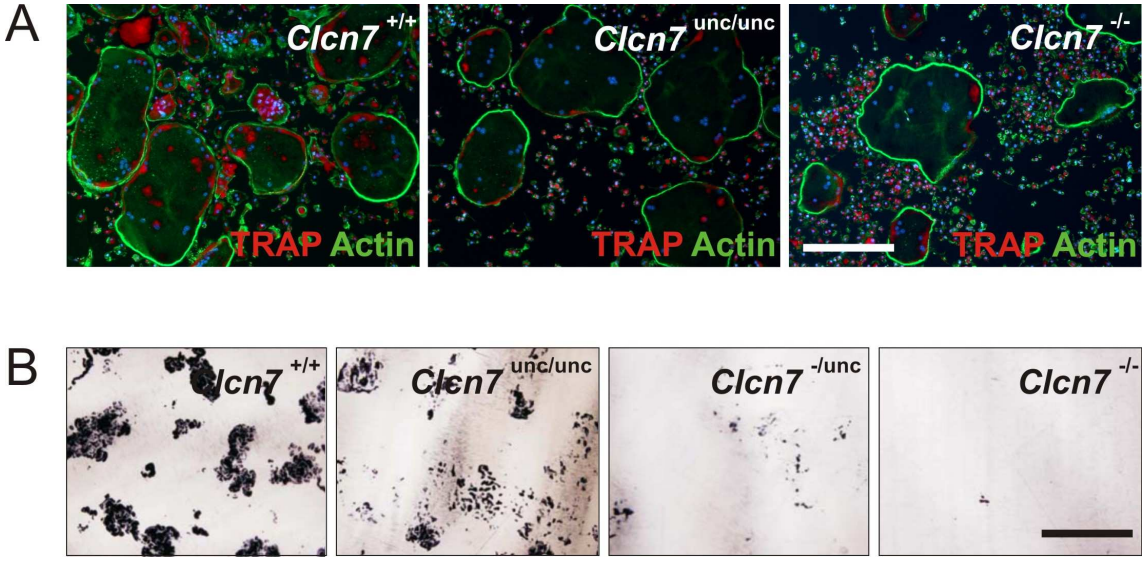

Fig. S6. Osteoclast phenotype of *Clcn7*$^{unc/unc}$ mice. (**A**) In vitro differentiated WT, *Clcn7*$^{unc/unc}$ *and Clcn7*$^{-/-}$ osteoclasts. All cells form sealing zones as indicated by the actin ring (green) and are positive for the osteoclast marker tartrate resistant acid phosphatase (TRAP, red). (**B**) Resorption pits formed by osteoclasts cultured on dentine visualized by Indian ink. *Clcn7*$^{unc/unc}$ osteoclasts form more pits than *Clcn7*$^{-/unc}$ osteoclasts but less than osteoclasts derived from WT littermates. Pits are only observed sporadically on *Clcn7*$^{-/-}$ cultured dentine. The mean area ± SEM resorbed by *Clcn7*$^{+/+}$, *Clcn7*$^{unc/unc}$, *Clcn7*$^{-/unc}$ and *Clcn7*$^{-/-}$ are 18.5% ± 1.2, 7.0% ± 1.1, 1.7% ± 0.2 and 0.1% ± 0.04, respectively. Scale bars: 200 µm (A) and 0.5 mm (B).

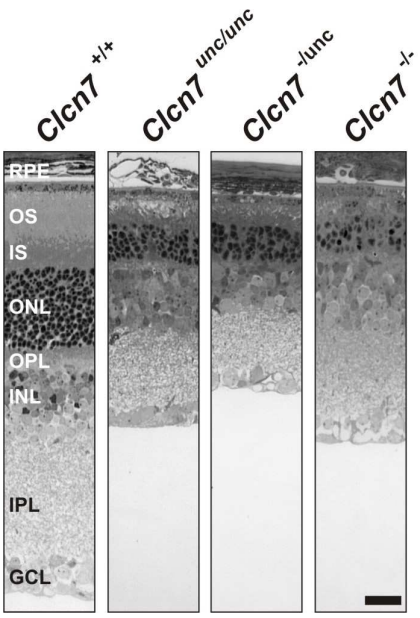

Fig. S7. Retinal degeneration in *Clcn7*$^{unc/unc}$ mice. Semi-thin sections of the retina. Degeneration of photoreceptor cells in the outer nuclear layer (ONL) and outer and inner segment (OS, IS, respectively) is similar in *Clcn7*$^{unc/unc}$, *Clcn7*$^{-/unc}$ and *Clcn7*$^{-/-}$ mice. RPE, retinal pigment epithelium; OS, photoreceptor outer segments; IS, photoreceptor inner segments; ONL, outer nuclear layer; OPL, outer plexiform layer; INL, inner nuclear layer; IPL, inner plexiform layer; GCL, ganglion cell layer. Scale bar: 25 µm.

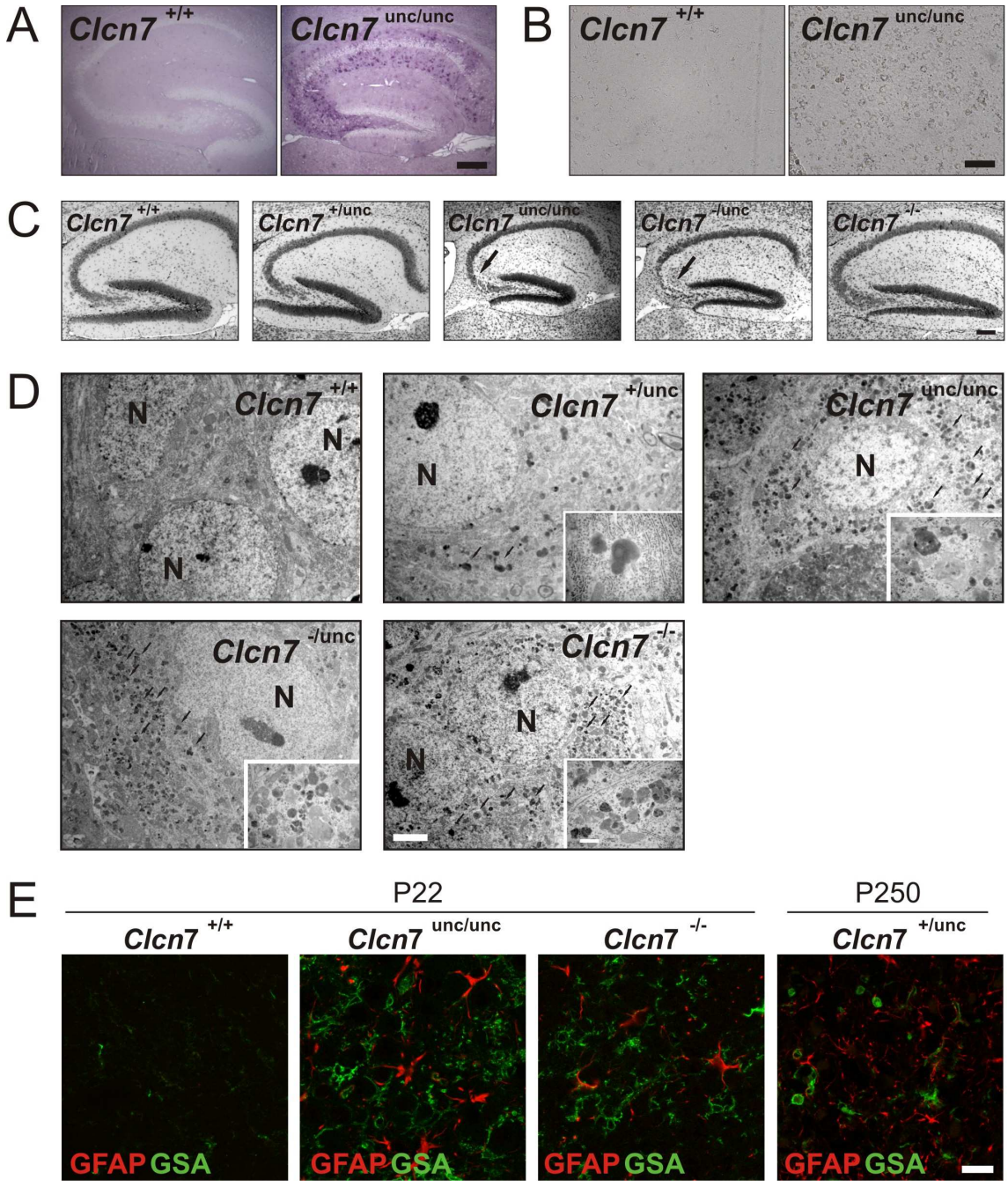

Fig. S8. Neuropathology in brains from *Clcn7*$^{unc/unc}$ and *Clcn7*$^{+/unc}$ mice. (**A**) PAS staining on paraffin sections reveals accumulation of carbohydrates in neurons of the hippocampus of P22 *Clcn7*$^{unc/unc}$ but not in WT mice. (**B**) Increased lysosomal acid phosphatase activity is visualized in situ as dark staining on cortex sections of P22 *Clcn7*$^{unc/unc}$ compared to WT mice. (**C**) Nissl staining indicates onset of neuronal loss of the hippocampal CA3 region in *Clcn7*$^{unc/unc}$ and *Clcn7*$^{-/unc}$ at P22 (arrows). At this age, degeneration is neither observed in *Clcn7*$^{+/unc}$ and WT controls, nor in *Clcn7*$^{-/-}$ mice. (**D**) Electron micrographs at P22 show lysosomal storage material (arrows) in cortical neurons of *Clcn7*$^{-/unc}$, *Clcn7*$^{unc/unc}$ and *Clcn7*$^{-/-}$ which is less abundant in the brain of *Clcn7*$^{+/unc}$ mice (N = nucleus). (**E**) Neurodegeneration in *Clcn7*$^{unc/unc}$ and *Clcn7*$^{-/-}$ mice at P22 and *Clcn7*$^{+/unc}$ at P250 is accompanied by microgliosis and

astrogliosis as revealed by increased staining with the microglial marker GSA (*Griffonia simplicifolia* agglutinin, green) and with an antibody against the glial fibrillary acidic protein (GFAP, red) in the cortex. Scale bars: 100 µm (A, B), 150 µm (C), 2 µm (D) and 500 nm (inset in D) and 20 µm (E).

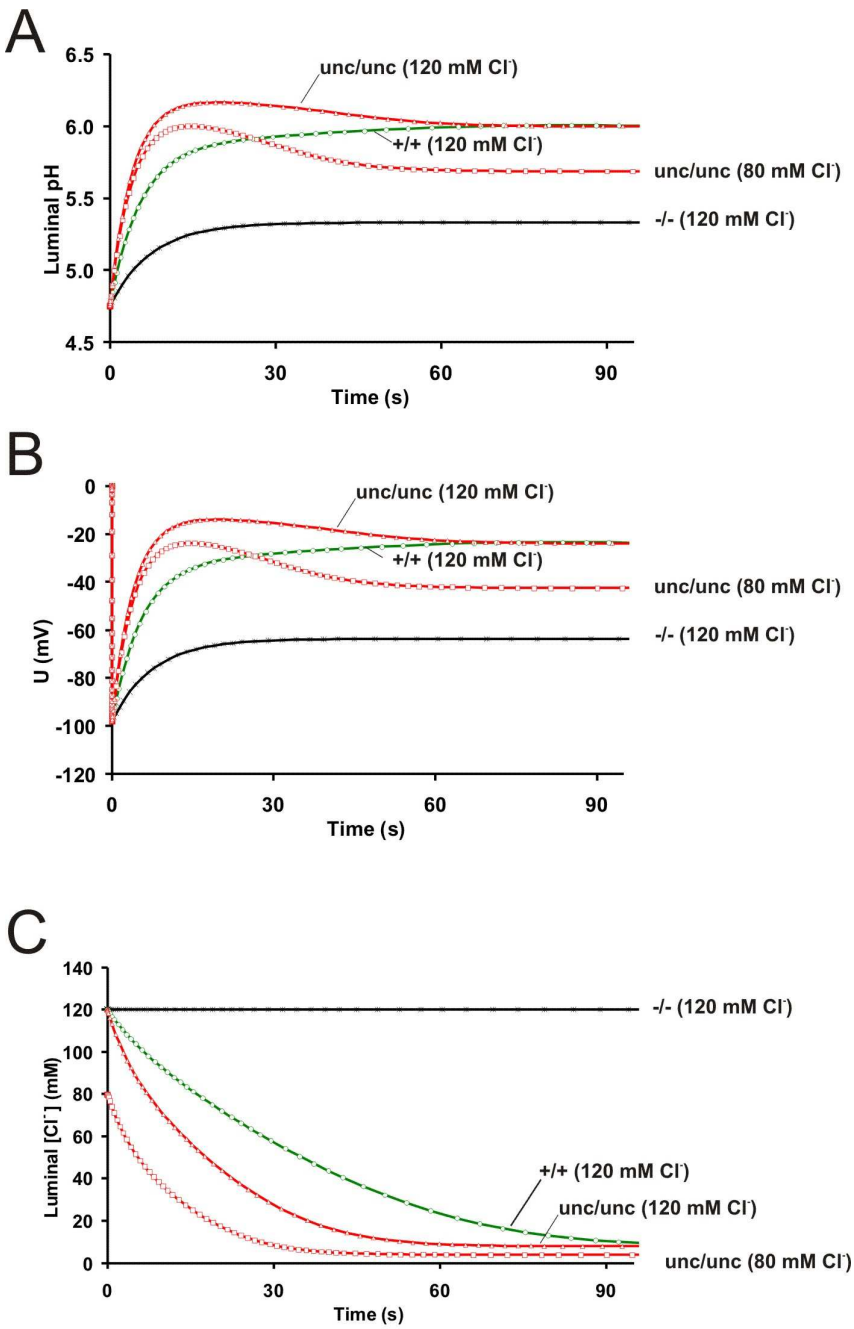

Fig. S9. Mathematical modeling of protonophore-induced lysosomal alkalinization. (**A**) Predicted vesicular pH, (**B**) predicted voltage (cytoplasm $\stackrel{def}{=}$ 0) and (**C**) predicted vesicular $[Cl^-]_i$ in the presence of a cation conductance and either a $2Cl^-/H^+$-exchanger (green), a Cl^- conductance (modeling CLC^{unc}, red) with identical starting $[Cl^-]_i$ (120 mM) or lower $[Cl^-]_i$ (80 mM), or without any Cl^- permeation (mimicking CLC KO, black). No H^+-ATPase activity was included, and the protonophore CCCP was mimicked by setting the H^+-conductance more than 10,000-fold higher than the cation or Cl^- conductance. Initial vesicular pH was set to 4.75 under all conditions (according to our measurements, Fig. 3D), and cytoplasmic pH to 6.4 (predicted from a plasma membrane voltage of -60 mV and pH_o=7.4 in the presence of a protonophore). With $[Cl^-]_i$ = 120 mM, the same value of pH_i is reached with either $2Cl^-/H^+$ exchange or a Cl^- conductance. This can also be deduced from

the Goldman-Hodgkin-Katz voltage equation for both Cl^- and H^+ at equilibrium in the presence of either a Cl^- conductance and an H^+ conductance or a Cl^-/H^+-exchanger (independent of its coupling rate) and an H^+ conductance. In both cases, pH_i is determined by $pH_i = pH_o + \log([Cl^-]_i/[Cl^-]_o)$.
In contrast to vesicles containing a $2Cl^-/H^+$-exchanger, the uncoupled Cl^- conductance predicts an overshoot in alkalinization, but only in the presence of a cation conductance. This was not observed experimentally with *Clcn7*$^{unc/unc}$ lysosomes (Fig. 3B). However, in that experiment CCCP had to cross the plasma membrane of intact cells to reach lysosomes. This leads to a gradual increase in H^+-conductance, in contrast to the instantaneous conductance used in the calculation. When introducing an H^+-conductance that increases with time into the model, the pH overshoot can be suppressed as expected (not shown). To account for the more acidic pH_l observed with CCCP/*Clcn7*$^{unc/unc}$ (Fig. 3B), a lower initial $[Cl^-]_i$ must be assumed. This is consistent with the predicted lower vesicular $[Cl^-]_i$ when proton-pump currents are neutralized by a Cl^- conductance (Fig. S10C). Because CCCP induces lysosomal alkalinization also in *Clcn7*$^{-/-}$ mice (Fig. 3B), lysosomes must contain other conductances that provide a countercurrent. The roughly similar alkalinization kinetics in the experiment of Fig. 3B suggests that this conductance has at least the same order of magnitude as those provided by ClC-7 or ClC-7^{unc}. The more acidic steady-state pH_l of *Clcn7*$^{-/-}$ lysosomes after CCCP-induced alkalinization indicates that it cannot be mediated by e.g. late endosomal ClC-3 (which partially shifts to lysosomal fractions in *Clcn7*$^{-/-}$ mice (*7*) nor by another Cl^- conductance. As substantial amounts of charge must be transferred to accompany the efflux of ~30 mM H^+ per pH unit, it is unlikely to be carried by Ca^{++}. Because cytosolic $[K^+]$ is at ~ 140 mM, an inside-out K^+ gradient cannot be large enough to create a luminal potential sufficiently negative to account for the measured acidic pH_l. We boldly propose that this could be a Na^+ conductance, with $[Na^+]_i$ being higher than in the cytosol, and being further increased during compensatory charge transfer for the H^+ efflux through CCCP. The resulting Na^+ diffusion potential (inside negative) (B) would cause a passive H^+-distribution with a luminal pH (A) that roughly corresponds to our experimental data (Fig. 3B). The presence of a substantial lysosomal cation conductance is suggested by experimental data obtained by van Dyke (*8*) and was found to be of similar magnitude as the anion conductance. However, it may not be selective for Na^+. The mechanism by which a lysosomal Na^+ gradient might be maintained is unclear. Hypothetically, it could be created by a vesicular Na^+/H^+-exchanger. In this respect, it is interesting to note that in yeast the single yeast CLC ScClC (gef1p) and the Na^+/H^+-exchanger Nhx1p are located in the same vesicular compartment and that their disruption leads to overlapping phenotypes (*13, 14*). Furthermore, four distinct mammalian NHE Na^+/H^+-antiport isoforms have been found in different vesicular compartments of mammalian cells, including endosomes, but apparently excluding lysosomes (*15*). Lysosomes, however, might receive continuously Na^+ from late endosomes. Another transporter discussed in modulating endosomal acidification is the Na^+,K^+-ATPase (*12, 16-18*), which may also raise vesicular Na^+-concentration.

The following parameters were used in eqs. (1) - (9):

Parameters set for initial conditions:

pH_i = 4.75; pH_o = 6.4; $[cat^+]_i$ = 100 mM; $[cat^+]_o$ = 10 mM; $[Cl^-]_i$ = 80 and 120 mM, respectively; $[Cl^-]_o$ = 20 mM; $[A^-]$ was calculated to set U = 0 mV at t=0.
Parameters set for transport:

g_{ATPase} = 0; g_{CLC} = 0 (for modeling CLC^{unc} and CLC KO, respectively) or 20 (CLC WT); $g_{Cl,\ cond}$ = 0 (CLC WT and CLC KO, respectively) or 60 (CLC^{unc}); $g_{H,\ cond}$ = 1,000,000 (mimicking CCCP); $g_{cat,\ cond}$ = 60.

Major conclusions from these calculations:

- difference in steady-state pH_l with CCCP between *Clcn7*$^{+/+}$ and *Clcn7*$^{unc/unc}$ could be explained by larger lysosomal [Cl^-] with exchanger, consistent with calculation of active acidification (Fig. S10)
- negative-inside potential created by protonophore-induced H^+ efflux could substantially activate ClC-7 even if it were as strongly rectifying as ClC-5 (*19*)

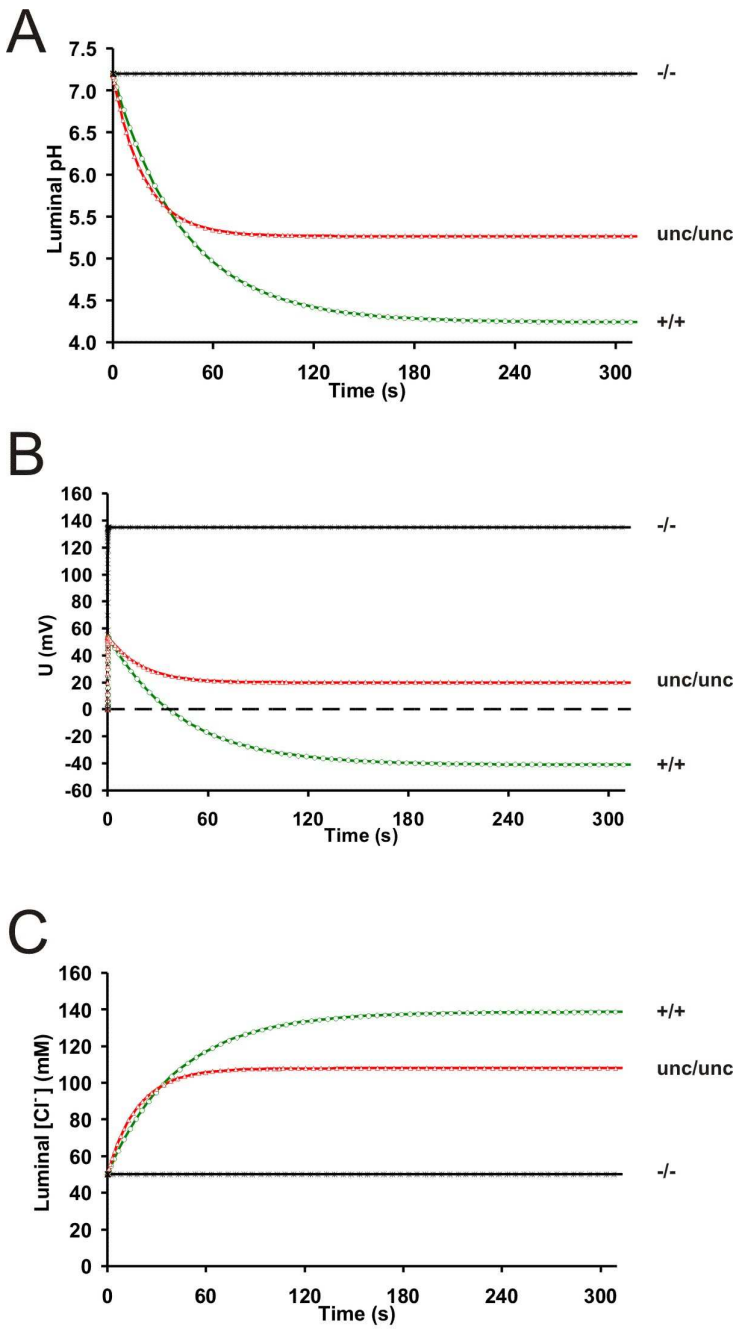

Fig. S10. Minimal mathematical model for ATP-dependent vesicle acidification. H^+ATPase-driven acidification modeled for a vesicle containing a proton pump, proton leak, and either no Cl^- conductance (black), a non-rectifying Cl^- conductance (as predicted for CLC^{unc} proteins, red), or a non-rectifying CLC $2Cl^-/H^+$-antiporter (green) as only membrane ion transport processes. (**A**) Calculated intravesicular pH, (**B**) calculated potential inside the vesicle (cytoplasm set to 0; note that this gives opposite polarity compared to plasma membrane voltage definition), (**C**) calculated intravesicular Cl^- concentration. Significant acidification occurs only when the pump current is neutralized by a countercurrent which in this minimal model is only mediated by either a $2Cl^-/H^+$-antiporter (green) or a Cl^- conductance (red). In accord with the literature (*12*), calculations (that we do not show) predicted that steady-state vesicular pH strongly depends on the ratio of pump activity to proton leak. We chose

a ratio that resulted in physiologically reasonable pH values. This was achieved by setting the proton leak to about one sixth of the total counterion conductance (comprising Cl^- and cations), consistent with previous reports (*20*). Interestingly, when electrical currents of the conductance and the $2Cl^-/H^+$-transporter are set to be roughly similar (as suggested for ClC-4 and -5 when compared at cytoplasmic positive voltages (*19, 21*)), vesicles containing the exchanger acidify even more than those containing an uncoupled Cl^- conductance, albeit with a slower acidification rate. Importantly, the presence of a Cl^- conductance on one hand and a $2Cl^-/H^+$-exchanger on the other hand make very different predictions as to the voltage: in the 'classical' picture of vesicular acidification (countercurrent through Cl^--channel), an inside-positive voltage is predicted (~+20 mV), whereas a $2Cl^-/H^+$-exchanger results in inside-negative voltages (~-40 mV) that would allow for an efficient operation of e.g. ClC-4 and ClC-5, which are strongly rectifying (*19, 21-23*). The differences in predicted voltage and pH_i are compatible with each other, since the more negative voltage decreases the electrical component of the electrochemical potential for protons. However, it conflicts with experimental data showing that the voltage of phagolysosomes is about +27 mV (*24*). It also clashes with experiments (*25, 26*) that used Di-S-C_3 fluorescence to estimate voltages in vesicle suspensions which demonstrated ATP-induced luminal accumulation of net positive charge. We conclude that the minimal model lacks essential components of real vesicles.
Importantly, our model predicts stronger luminal chloride accumulation in the presence of a $2Cl^-/H^+$-exchanger, which agrees with our experimental data (Fig. 3E). Further simulations we do not show here predict that the presence of a cation conductance accelerates acidification kinetics and moderately changes the predicted steady-state pH, but does not change the prediction of inverted membrane potentials when comparing chloride conductance and chloride/proton exchange.

The following parameters were used in eqs. (1)- (9):

Parameters set for initial conditions:
pH_i = 7.2; pH_o = 7.2; $[cat^+]_i$ = 140 mM; $[cat^+]_o$ = 140 mM; $[Cl^-]_i$ = 50 mM; $[Cl^-]_o$ = 50 mM; $[A^-]$ was calculated to set U = 0 mV at t=0.

Parameters set for transport:
g_{ATPase} = 20; g_{CLC} = 0 (for modeling CLC^{unc} and CLC KO, respectively) or 20 (CLC WT); $g_{Cl,\ cond}$ = 0 (CLC WT and CLC KO, respectively) or 60 (CLC^{unc}); $g_{H,\ cond}$ = 20; $g_{cat,\ cond}$ = 0.

Major predictions from the minimal model:

- in the absence of rectification, $2Cl^-/H^+$-exchange supports acidification at least as efficiently as an uncoupled Cl^- conductance
- vesicular voltage inside-positive with conductance, but negative with exchanger
- substantially higher $[Cl^-]_i$ with exchanger than with conductance

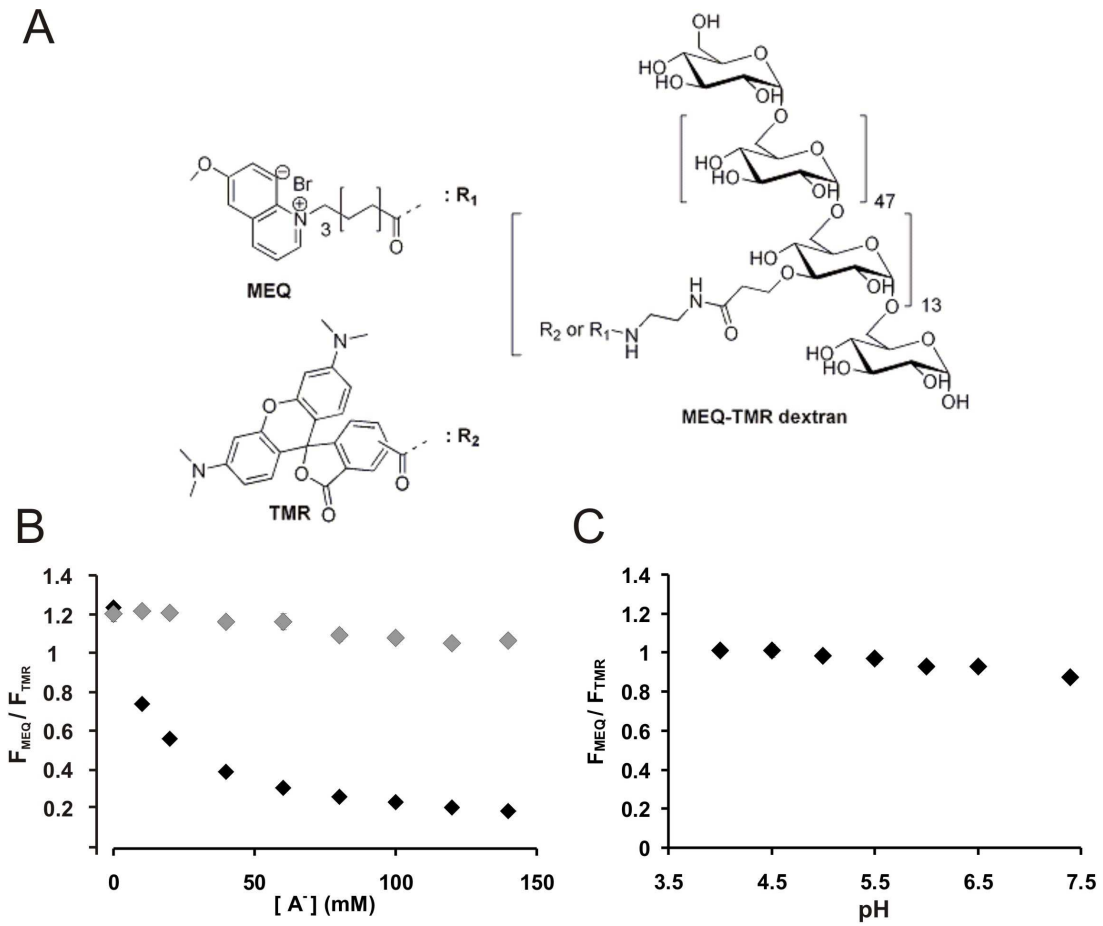

Fig. S11. Ratioable Cl^--sensitive dye and its characterization in vitro. (**A**) Chemical structure of MEQ/TMR-dextran. On average, one dextran molecule (~10 kDa) is coupled to 13 fluorescent moieties (mixture of MEQ and TMR). Fluorescence of MEQ is quenched by Cl^- (*10*) whereas the Cl^--insensitive fluorescence of TMR serves as reference. (**B**) MEQ/TMR fluorescence ratio was monitored upon addition of sodium salts of the anions (A^-) Cl^- (black) and gluconate (gray). Addition of NaCl selectively quenches fluorescence of the MEQ moiety and thus decreases the fluorescence ratio. Note that the dye responds very poorly to further increases of [Cl^-] above ~60 mM Cl^-. (**C**) MEQ/TMR-fluorescence ratios were virtually unaffected by pH between pH 4 to 7.4. Error bars (only shown when larger than symbols) represent SEM.

Table S1. Summary of phenotypes of ClC-7 mutants.

Phenotype	**+/+**	**+/-**	**+/unc**	**unc/unc**	**-/unc**	**-/-**
Growth	normal	normal	normal	retarded	retarded	retarded
Ostm1 level	normal	normal	n.d.	normal	normal	down
Osteopetrosis	no	no	n.d.	mild	medium	severe
Neuropathology	no	no	late onset	severe	severe	severe
Coat color (agouti)	brown	brown	brown	brown	brown	gray

(n.d., not determined)

Supporting References

1. U. Kornak *et al.*, Loss of the ClC-7 chloride channel leads to osteopetrosis in mice and man. *Cell* **104**, 205 (2001).
2. N. Chalhoub *et al.*, Grey-lethal mutation induces severe malignant autosomal recessive osteopetrosis in mouse and human. *Nat Med* **9**, 399 (2003).
3. F. W. Farley, P. Soriano, L. S. Steffen, S. M. Dymecki, Widespread recombinase expression using FLPeR (flipper) mice. *Genesis* **28**, 106 (2000).
4. P. F. Lange, L. Wartosch, T. J. Jentsch, J. C. Fuhrmann, ClC-7 requires Ostm1 as a β-subunit to support bone resorption and lysosomal function. *Nature* **440**, 220 (2006).
5. W. Günther, A. Lüchow, F. Cluzeaud, A. Vandewalle, T. J. Jentsch, ClC-5, the chloride channel mutated in Dent's disease, colocalizes with the proton pump in endocytotically active kidney cells. *Proc Natl Acad Sci U S A* **95**, 8075 (1998).
6. T. Maritzen, D. J. Keating, I. Neagoe, A. A. Zdebik, T. J. Jentsch, Role of the vesicular chloride transporter ClC-3 in neuroendocrine tissue. *J Neurosci* **28**, 10587 (2008).
7. M. Poët *et al.*, Lysosomal storage disease upon disruption of the neuronal chloride transport protein ClC-6. *Proc Natl Acad Sci U S A* **103**, 13854 (2006).
8. R. W. Van Dyke, Acidification of rat liver lysosomes: quantitation and comparison with endosomes. *Am J Physiol* **265**, C901 (1993).
9. S. Meyer, S. Savaresi, I. C. Forster, R. Dutzler, Nucleotide recognition by the cytoplasmic domain of the human chloride transporter ClC-5. *Nat Struct Mol Biol* **14**, 60 (2007).
10. J. Biwersi, A. S. Verkman, Cell-permeable fluorescent indicator for cytosolic chloride. *Biochemistry* **30**, 7879 (1991).
11. S. L. Rybak, F. Lanni, R. F. Murphy, Theoretical considerations on the role of membrane potential in the regulation of endosomal pH. *Biophys J* **73**, 674 (1997).
12. M. Grabe, G. Oster, Regulation of organelle acidity. *J Gen Physiol* **117**, 329 (2001).
13. R. A. Gaxiola *et al.*, The *Arabidopsis thaliana* proton transporters, AtNhx1 and Avp1, can function in cation detoxification in yeast. *Proc Natl Acad Sci U S A* **96**, 1480 (1999).
14. K. Bowers, B. P. Levi, F. I. Patel, T. H. Stevens, The sodium/proton exchanger Nhx1p is required for endosomal protein trafficking in the yeast *Saccharomyces cerevisiae*. *Mol Biol Cell* **11**, 4277 (2000).
15. N. Nakamura, S. Tanaka, Y. Teko, K. Mitsui, H. Kanazawa, Four Na^+/H^+ exchanger isoforms are distributed to Golgi and post-Golgi compartments and are involved in organelle pH regulation. *J Biol Chem* **280**, 1561 (2005).
16. C. C. Cain, D. M. Sipe, R. F. Murphy, Regulation of endocytic pH by the Na^+,K^+-ATPase in living cells. *Proc Natl Acad Sci U S A* **86**, 544 (1989).
17. R. Fuchs, S. Schmid, I. Mellman, A possible role for Na^+,K^+-ATPase in regulating ATP-dependent endosome acidification. *Proc Natl Acad Sci U S A* **86**, 539 (1989).
18. K. Teter *et al.*, Cellubrevin-targeted fluorescence uncovers heterogeneity in the recycling endosomes. *J Biol Chem* **273**, 19625 (1998).

19. T. Friedrich, T. Breiderhoff, T. J. Jentsch, Mutational analysis demonstrates that ClC-4 and ClC-5 directly mediate plasma membrane currents. *J Biol Chem* **274**, 896 (1999).
20. H. Barriere *et al.*, Revisiting the Role of CFTR and Counterion Permeability in the pH Regulation of Endocytic Organelles. *Mol Biol Cell*, 3125 (2009).
21. K. Steinmeyer, B. Schwappach, M. Bens, A. Vandewalle, T. J. Jentsch, Cloning and functional expression of rat CLC-5, a chloride channel related to kidney disease. *J Biol Chem* **270**, 31172 (1995).
22. O. Scheel, A. Zdebik, S. Lourdel, T. J. Jentsch, Voltage-dependent electrogenic chloride proton exchange by endosomal CLC proteins. *Nature* **436**, 424 (2005).
23. A. Picollo, M. Pusch, Chloride / proton antiporter activity of mammalian CLC proteins ClC-4 and ClC-5. *Nature* **436**, 420 (2005).
24. B. E. Steinberg, N. Touret, M. Vargas-Caballero, S. Grinstein, *In situ* measurement of the electrical potential across the phagosomal membrane using FRET and its contribution to the proton-motive force. *Proc Natl Acad Sci U S A* **104**, 9523 (2007).
25. R. Fuchs, P. Mâle, I. Mellman, Acidification and ion permeabilities of highly purified rat liver endosomes. *J Biol Chem* **264**, 2212 (1989).
26. S. Ohkuma, Y. Moriyama, T. Takano, Electrogenic nature of lysosomal proton pump as revealed with a cyanine dye. *J Biochem* **94**, 1935 (1983).